

Laplacian Scale-Space Behavior of Planar Curve Corners

Xiaohong Zhang, Ying Qu, Dan Yang, Hongxing Wang, and Jeff Kymer

Abstract—Scale-space behavior of corners is important for developing an efficient corner detection algorithm. In this paper, we analyze the scale-space behavior with the Laplacian of Gaussian (LoG) operator on a planar curve which constructs Laplacian Scale Space (LSS). The analytical expression of a Laplacian Scale-Space map (LSS map) is obtained, demonstrating the Laplacian Scale-Space behavior of the planar curve corners, based on a newly defined unified corner model. With this formula, some Laplacian Scale-Space behavior is summarized. Although LSS demonstrates some similarities to Curvature Scale Space (CSS), there are still some differences. First, no new extreme points are generated in the LSS. Second, the behavior of different cases of a corner model is consistent and simple. This makes it easy to trace the corner in a scale space. At last, the behavior of LSS is verified in an experiment on a digital curve.

Index Terms—Corner detection, Laplacian of Gaussian, planar curve, scale space

1 INTRODUCTION

SINCE scale-space theory was developed by Witkin [1], Koenderink [2], Yuille [3], Lindeberg [4] and Florack [5], it has become a well-founded framework for problems in image processing and computer vision, such as object recognition [6], [7], [8], [9], image registration [10], shape matching [11], [12], [13], shape representation [14], [15], [16], feature detection [17], [18]. Particularly, the scale-space technique has been extensively utilized in corner detection in the past two decades, e.g., [19], [20], [21], [22], [23], [24], [25], [26]. It is necessary to figure out the scale-space behavior of corners. For example, how the extreme points, corresponding to corners at each scale, of a corner detector move and whether they will persist, vanish or merge as the scale varies. Such behavior makes it difficult to select an appropriate scale on which a corner detector is used. However, an inappropriate scale will then largely affect the performance of the corner detector.

In this work, our interest lies in the scale-space behavior of planar curves corners. The related research can be traced back to the work of Rattarangsi and Chin on CSS corner

detector [19]. The basic methodology is to construct the scale-space map and analyze the trajectories of extreme points in scale space. The scale-space map consists of the extreme points of curvature at all scales. Three typical corner models are used, that is, the isolated single corner model (Γ model) and the isolated double corner model (END model, STAIR model). Rattarangsi and Chin's work was later improved by Zhong [27]. Zhong showed that Rattarangsi and Chin had failed to take into account the shrinkage effect of the evolved curve and hence rebuilt the CSS theory using the same methodology. Since the structure of the CSS operator is complex, both Rattarangsi and Zhong merely provided an equation for each of the three corner models. No more precise results were presented in their papers. Zhong [28], [29] also studied the scale-space behavior of corners with the Direct Curvature Scale-Space (DCSS) corner detector in a similar methodology. Instead of constructing the scale space by evolving the curve and calculating the curvature as in the CSS, the DCSS is constructed by evolving the curvature of the curve directly. To sum up, the above-mentioned research considered only corner detectors based on the curvature of a planar curve. In fact, the CSS and the DCSS adopt two different parametric representations of a planar curve. The DCSS computes the curvature of the planar curve by $\dot{\varphi}(s)$ whereas the CSS by $[\dot{x}(s)\ddot{y}(s) - \ddot{x}(s)\dot{y}(s)]/[(\dot{x}(s)^2 + \dot{y}(s)^2)^{3/2}]$. There are also many scale-space corner detectors based on other measures [22], [24], [30], [31], [32]. As far as we know, none of them analyze scale-space behavior.

In this work, we intended to explore the scale-space behavior of corners with the Difference of Gaussian (DoG) corner detector [24]. This is a scale-space corner detector based on the DoG operator and has comparable detection performance to the CSS. Though the authors proved that the DoG detector has the same extreme points as the CSS, their result was obtained under the same assumption as Rattarangsi [19]. In other words, the DoG detector does not have the same extreme points as the CSS when the curves

- X. Zhang is with the Key Laboratory of Dependable Service Computing in Cyber Physical Society Ministry of Education, Chongqing 400044, PR China, with the School of Software Engineering, Chongqing University, Chongqing 401331, PR China, and is also with the State Key laboratory of Coal Mine Disaster Dynamics and Control, Chongqing 400044, PR China. E-mail: xhonz@cqu.edu.cn.
- Y. Qu is with College of Computer Science, Chongqing University, Chongqing 400044, PR China. E-mail: ying.qu@cqu.edu.cn.
- D. Yang and J. f Kymer is with School of Software Engineering, Chongqing University, Chongqing 401331, PR China. E-mail: dyang@cqu.edu.cn, kymer@industrialfun.com.
- H. Wang is with the School of Electrical and Electronic Engineering, Nanyang Technological University, Singapore 639798. E-mail: ihxwang@ntu.edu.sg.

Manuscript received 22 Feb. 2014; revised 15 Oct. 2014; accepted 6 Jan. 2015.
Date of publication 22 Jan. 2015; date of current version 7 Oct. 2015.

Recommended for acceptance by L. Zelnik-Manor.

For information on obtaining reprints of this article, please send e-mail to: reprints@ieee.org, and reference the Digital Object Identifier below.

Digital Object Identifier no. 10.1109/TPAMI.2015.2396074

evolves. Thus, it is still unknown that what scale-space behavior of corners with the DoG operator is and whether it has some new features. This work will help future researchers in improving the DoG corner detector and devising more powerful algorithms. Unfortunately, it is difficult to investigate the scale-space behavior of corners with the DoG detector due to its complexity. Our aim in this paper, therefore, is to perform an analysis of the scale-space behavior of corners with LoG operator which approximates the DoG operator, i.e., $DoG_\sigma(s) \approx (k-1)\sigma^2 LoG_\sigma(s)$, $k \neq 1$, $k \in \mathbb{Z}^+$. Here, k is the constant multiplicative factor which separates the two nearby scales σ and $k\sigma$ in the DoG operator. When k goes to one, the approximation error will go to zero. It should be pointed out, that the Laplacian operator in our work is defined on a planar curve rather than a gray scale image, on which all of the previous Laplacian operators were defined [33], [34], [35], [36], [37], [38], [39].

Inspired by the CSS [19], [27], the coordinate functions $x(s)$, $y(s)$ of a curve is first convolved with a LoG operator to construct the LSS. Secondly, the extreme points of the 2-norm of the evolved coordinate functions at each scale are plotted on the $s - \sigma$ plane to construct the scale-space map, which is referred to as a LSS map. Finally, the scale-space behavior of corners with the LoG operator is summarized by analyzing the LSS maps of corner models. In contrast to the CSS, we do not use the three typical corner models in our analysis. Actually, only one model is exploited, resulting from redefining the END model to include the Γ model and the STAIR model. We call this corner model the unified corner model. As a consequence, the Laplacian Scale-Space behavior of corners can be expressed in a single formula as opposed to the formulas for the three corner models in the CSS theory. Furthermore, mathematical expressions of several key points are derived, for example the location where two adjacent corners merge, the location where a strong corner persists, and the location where a weak corner vanishes. These locations were not obtained in either Rattarangsi's work or in Zhong's.

The paper is organized as follows. In Section 2, the LSS is established. Section 3 details the properties of the LSS map. Digital scale space and an example of the application of the scale-space properties on corner detection are presented in Section 4. The paper is concluded in Section 5.

2 PRELIMINARIES

In this section, we first formulate the LoG operator of a planar curve and then construct the Laplacian Scale-Space theory.

2.1 Laplacian Scale-Space

Let

$$C(s) = (x(s), y(s)) \quad (1)$$

represent a planar curve, where s is a path length along the curve. Define the LoG operator as

$$LoG_\sigma(s) = \nabla^2 g_\sigma(s). \quad (2)$$

Here, $g_\sigma(s)$ denotes a Gaussian function with a zero-mean and the standard deviation σ . ∇ denotes the gradient

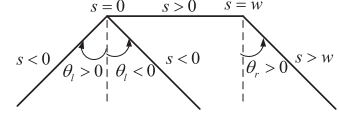


Fig. 1. The unified corner model.

operator. Then we get the LSS by convolving the original curve (1) with a LoG operator (2)

$$LoG_\sigma(s) * c(s) = (\nabla^2 g_\sigma(s) * x(s), \nabla^2 g_\sigma(s) * y(s)). \quad (3)$$

Define the response function of the LoG operator according to the 2-norm as

$$M_\sigma(s) = [\nabla^2 g_\sigma(s) * x(s)]^2 + [\nabla^2 g_\sigma(s) * y(s)]^2. \quad (4)$$

A LSS map is then defined as the extreme points of the response function at all scales. To construct the LSS map, we just need acquire s at scale σ by solving

$$\dot{M}_\sigma(s) = 0, \quad (5)$$

where

$$\dot{M}_\sigma(s) = \frac{\partial M_\sigma(s)}{\partial s}. \quad (6)$$

However, we are only interested in the maximums of $M_\sigma(s)$ which correspond to the corners at each scale. These maximums are determined by

$$\dot{M}_\sigma(s) = 0, \ddot{M}_\sigma(s) < 0, \quad (7)$$

where

$$\ddot{M}_\sigma(s) = \frac{\partial^2 M_\sigma(s)}{\partial s^2}. \quad (8)$$

2.2 Theorem

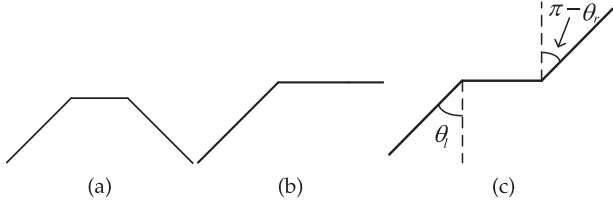
In this subsection, we will present the main result of this paper. The goal is to apply the LoG operator on a corner model to derive the analytical expression of the LSS map.

In the works of Rattarangsi and Chin [19] and Zhong [28], [27], the Γ model, the END model, and the STAIR model are separately analyzed. Instead, we define the unified corner model incorporates all three models, which helps us obtain a general expression of the LSS map. This corner model is written as

$$x(s) = \begin{cases} s \sin \theta_l, & s < 0 \\ s, & 0 \leq s < w \\ (s-w) \sin \theta_r + w, & s \geq w, \end{cases} \quad (9)$$

$$y(s) = \begin{cases} s \cos \theta_l & s < 0 \\ 0 & 0 \leq s < w \\ -(s-w) \cos \theta_r + w & s \geq w. \end{cases}$$

Fig. 1 is an illustration of the unified corner model with two corners and a corner separation w . The two corners are located on $s = 0$ and $s = w$. The model is symmetric with respect to $s = 0.5w$. When the ray with $s < 0$ lies on the dashed line, $\theta_l = 0$; when θ_l increases it turns clockwise, $\theta_l > 0$; when decreasing it turns counter-clockwise, $\theta_l < 0$. For the ray with $s > w$, the definition is the just the opposite. Without loss of generality, we assume $\theta_l \in (-\pi/2, \pi/2)$.


 Fig. 2. (a) END model. (b) Γ model. (c) STAIR model.

When $\theta_r \in (-\pi/2, \pi/2)$, the corner model is an END model, shown in Fig. 2a; when $\theta_r = \pi/2$, Γ model, shown in Fig. 2b; when $\theta_r \in (\pi/2, 3\pi/2)$, the STAIR model, shown in Fig. 2c. For the STAIR model, $\pi - \theta_r$ is actually more intuitive than θ_r . $\pi - \theta_r$ is shown in Fig. 2c. When say the END model is equiangular, we mean $\theta_l = \theta_r$. When articulating that the STAIR model is equiangular, we mean $\theta_l = \pi - \theta_r$.

By substituting (9) into \dot{M}_σ and \ddot{M}_σ , we rewrite them as

$$\dot{M}_\sigma(s) = -\frac{1}{\sigma^2} \{ 2\alpha g_\sigma^2(s) + \beta(2s-w)g_\sigma(s)g_\sigma(s-w) \} \quad (10)$$

and

$$\begin{aligned} \ddot{M}_\sigma(s) = & -\frac{1}{\sigma^2} \left\{ \alpha \left(2 - \frac{4s^2}{\sigma^2} \right) g_\sigma^2(s) \right. \\ & + \beta \left[2 - \frac{(2s-w)^2}{\sigma^2} \right] g_\sigma(s)g_\sigma(s-w) \\ & \left. + \gamma \left[2 - \frac{4(s-w)^2}{\sigma^2} \right] g_\sigma^2(s-w) \right\}, \end{aligned} \quad (11)$$

where

$$\alpha = 1 - \sin \theta_l, \gamma = 1 - \sin \theta_r, \theta = \frac{\theta_l + \theta_r}{2}, \beta = 2 \sin \theta \sqrt{\alpha\gamma}. \quad (12)$$

By solving $\dot{M}_\sigma(s) = 0$, we obtain the analytical expression of the LSS map of an unified corner model. See the Appendix for more details.

Theorem 2.1. For an isolated unified corner model with a corner separation w , its LSS map is mathematically expressed as:

- 1) When $\theta_r = \pi/2$, $s = 0$.
- 2) When $\theta_r \neq \pi/2$ and $\theta_l \neq \theta_r$,

$$\sigma^2 = \frac{(w-2s)w}{2 \ln \left[\sqrt{\frac{1-\sin \theta_r}{1-\sin \theta_l} \frac{(w-2s) \sin \theta \pm \sqrt{(w-2s)^2 \sin^2 \theta - 4s(s-w)}}{2s}} \right]}; \quad (13)$$

- 3) When $\theta_r \neq \pi/2$ and $\theta_l = \theta_r$, $s = 0.5w$ is also included besides (13).

To simplify discussions, define

$$F_1(s) \triangleq \frac{(w-2s)w}{2 \ln \left[\sqrt{\frac{1-\sin \theta_r}{1-\sin \theta_l} \frac{(w-2s) \sin \theta + \sqrt{(w-2s)^2 \sin^2 \theta - 4s(s-w)}}{2s}} \right]}, \quad (14)$$

$$F_2(s) \triangleq \frac{(w-2s)w}{2 \ln \left[\sqrt{\frac{1-\sin \theta_r}{1-\sin \theta_l} \frac{(w-2s) \sin \theta - \sqrt{(w-2s)^2 \sin^2 \theta - 4s(s-w)}}{2s}} \right]}. \quad (15)$$

Theorem 2.1 indicates that the LSS map of the unified corner model can be determined analytically, which allows us to derive properties from its expressions. These expressions demonstrate the extreme points and the scales where the extreme points may exist. By drawing them all on (s, σ) plane, we acquire the LSS map.

As we can see from the theorem, to determine the expressions of the LSS map, we need to determine the domains of $\sigma^2 = F_1(s)$ and $\sigma^2 = F_2(s)$ which vary when θ_l , θ_r , and w varies. These denote the range of the probable location of the response function's extreme points at all scales. In other words, the trajectories of the corners in the LSS are bounded by the definitional domains. In the following, we will investigate the domains of $F_1(s)$ and $F_2(s)$.

Denote

$$\begin{aligned} \chi &= -(s-0.5w)w, \Delta = (w-2s)^2 \sin^2 \theta - 4s(s-w), \\ \eta &= \sqrt{\frac{\gamma}{\alpha}}, \varphi \triangleq \frac{\chi \sin \theta + \sqrt{\Delta}}{s}, \psi \triangleq \frac{\chi \sin \theta - \sqrt{\Delta}}{s}. \end{aligned} \quad (16)$$

Let's begin with $F_1(s)$. Apparently, $\Delta \geq 0$ while the denominator $\ln \varphi$ and the numerator χ of $F_1(s)$ must have the same sign since $F_1(s)$ is nonnegative. We get the inequality

$$\begin{cases} \Delta \geq 0 \\ \varphi > 1 \\ \chi > 0 \end{cases} \quad \text{or} \quad \begin{cases} \Delta \geq 0 \\ 0 < \varphi < 1 \\ \chi < 0 \end{cases}. \quad (17)$$

Similarly to $F_1(s)$, for $F_2(s)$ we get

$$\begin{cases} \Delta \geq 0 \\ \psi > 1 \\ \chi > 0 \end{cases} \quad \text{or} \quad \begin{cases} \Delta \geq 0 \\ 0 < \psi < 1 \\ \chi < 0 \end{cases}. \quad (18)$$

Solve them and we get the domains of $F_1(s)$ and $F_2(s)$. Refer to the Appendix for more details.

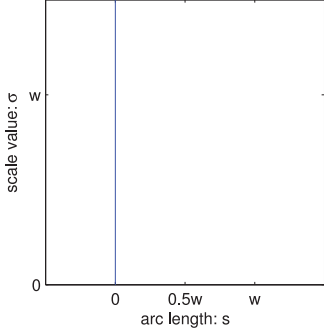
Consequently, we are able to determine the LSS map of the unified corner model. It can be seen from (13) that the variation of θ_l and θ_r changes the definitional domains. This then causes differences in the LSS map. Note that since θ_l and θ_r change continuously, the LSS map will also vary continuously. To understand the scale-space behavior of corners with the LSS, we need to investigate the LSS map of the unified corner model with different θ_l and θ_r . We will analyze these separately in the next section with the help of the above conclusions.

Theorem 2.2. The LSS maps of two isolated unified corner models with corner separations w_i and w_j are linearly related by the ratio w_i/w_j .

Furthermore, we get Theorem 2.2 showing the effect of w on the LSS map with fixed θ_l and θ_r . Theorem 2.2 indicates that w has no effect on the structure of the LSS map and can be utilized as the unit of plane $s - \sigma$. In the next section, all of the corner models have the same corner separation w .

3 LAPLACIAN SCALE-SPACE THEORY

In this section, we will discuss properties of the LSS map of the unified corner model in detail, i.e., the effect of the

Fig. 3. The LSS map of the Γ model.

corner angles θ_l and θ_r on the LSS map. To simplify our discussion, we present our results on the Γ model, the END mode and the STAIR model separately.

3.1 Γ Model

From Theorem 2.1, we can see that the LSS map of a Γ model is produced by $s = 0$ which is independent of θ_l and σ . It is easily verified that $\ddot{M}_\sigma < 0$ at $s = 0$. In other words, $M_\sigma(s)$ reaches its maximum at $s = 0$. We draw the LSS map as shown in Fig. 3.

Property 3.1. *For the isolated Γ model with a corner separation w , the trajectory of the corner locates at $s = 0$ for all scales.*

3.2 END Model

Without loss of generality, let $-\pi/2 < \theta_l \leq \theta_r < \pi/2$. From Theorem 2.1 and the domains of $\sigma^2 = F_1(s)$ and $\sigma^2 = F_2(s)$, we get the following corollary which formulates the distribution of the LoG extreme points of the END model on plane $s - \sigma$.

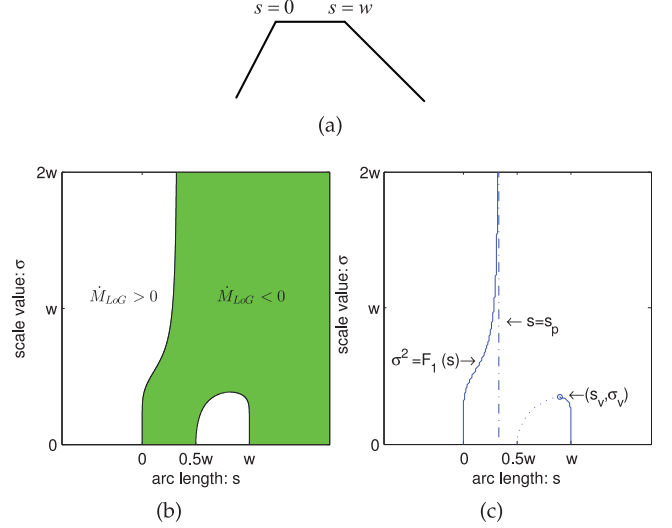
Corollary 3.2. *For the isolated END model with a corner separation w and $-\pi/2 < \theta_l \leq \theta_r < \pi/2$, its LSS map is analytically determined by:*

$$1) \quad \text{as } 0 \leq \theta_l + \theta_r < \pi, \\ \sigma^2 = F_1(s), \quad s \in (0, s_p) \cup (0.5w, w); \quad (19)$$

$$2) \quad \text{as } 0 < \theta_l = \theta_r < \pi/2, \\ \sigma^2 = F_1(s), \quad s \in (0, 0.5w) \cup (0.5w, w) \\ \sigma^2 = (0, +\infty), \quad s = 0.5w; \quad (20)$$

$$3) \quad \text{as } -\pi < \theta_l + \theta_r < 0, \\ \sigma^2 = F_1(s), \quad s \in [s_a, 0) \cup (0, s_p) \cup (0.5w, w) \cup (w, s_b] \\ \sigma^2 = F_2(s), \quad s \in [s_a, 0) \cup (w, s_b]; \quad (21)$$

$$4) \quad \text{and as } -\pi/2 < \theta_l = \theta_r < 0, \\ \sigma^2 = F_1(s), \quad s \in [s_a, 0) \cup (0, 0.5w) \cup (0.5w, w) \cup (w, s_b] \\ \sigma^2 = F_2(s), \quad s \in [s_a, 0) \cup (w, s_b] \\ \sigma^2 = (0, +\infty), \quad s = 0.5w. \quad (22)$$

Fig. 4. (a) The END model with $0 \leq \theta_l + \theta_r < \pi$ and $-\pi/2 < \theta_l < \theta_r < \pi/2$. (b) The distribution of $\ddot{M}_\sigma(s)$. (c) The LSS map.

where

$$\begin{aligned} s_p &= \frac{w}{2} \left(1 + \frac{\sin \frac{\theta_l + \theta_r}{2}}{\cos \frac{\theta_l + \theta_r}{2}} \right), \\ s_a &= \frac{w}{2} \left(1 - \frac{1}{\cos \theta} \right), \\ s_b &= \frac{w}{2} \left(1 + \frac{1}{\cos \theta} \right), \\ \theta &= \frac{\theta_l + \theta_r}{2}. \end{aligned} \quad (23)$$

It can be seen from Corollary 3.2 that the LSS map is generated by $F_1(s)$ in the case where $0 \leq \theta_l + \theta_r < \pi$, $-\pi/2 < \theta_l < \theta_r < \pi/2$. Here, the LSS map is obtained by drawing $F_1(s)$ with $s \in (0, s_p) \cup (0.5w, w)$ on the plane $s - \sigma$, as shown in Fig. 4c. Actually, the LSS map here consists of two categories of trajectories. The solid lines in Fig. 4c represent one category denoting the trajectories of the corners $s = 0$ and $s = w$ in scale space. The other category, represented by the curved dashed line in Fig. 4c, indicates the trajectories of the LoG minimums. This is proved by checking the changes of $\ddot{M}_\sigma(s)$ along the s -axis. This is shown in Fig. 4b which displays the distribution of $\ddot{M}_\sigma(s)$ on the plane $s - \sigma$. The shaded region and the unshaded regions in Fig. 4b correspond to $\ddot{M}_\sigma(s) < 0$ and $\ddot{M}_\sigma(s) > 0$, respectively. Obviously, the points on the solid lines have $\ddot{M}_\sigma(s) < 0$ and the points on dashed line have $\ddot{M}_\sigma(s) > 0$. That is, the points on the solid lines represent the maximum of $M_\sigma(s)$ and the points on the dashed lines represent the minimum points of $M_\sigma(s)$. In the following cases of the unified corner model, we will omit the process of generating the LSS map from the corollary since the process is the same as the one described here. The solid lines will always denote the maximums of $M_\sigma(s)$ and the dashed lines the minimums of $M_\sigma(s)$.

It is easily seen from Fig. 4c that $F_1(s)$ increases monotonically on $(0, s_p) \cup (0.5w, s_r)$ and decreases monotonically on (s_r, w) . The trajectory of the corner $s = 0$ approaches $s = s_p$ as the scale increases and persists at all scales on $(0, s_p)$. Meanwhile, the trajectory of the corner $s = w$ moves towards the midpoint of the model on (s, w) and meets the

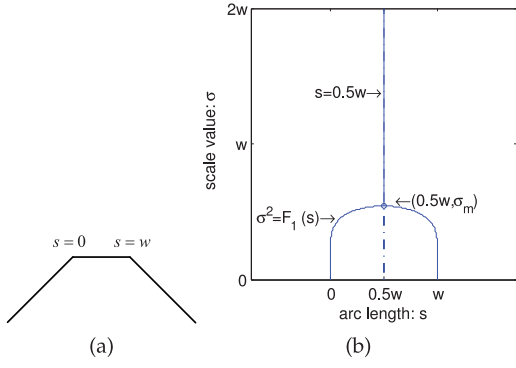


Fig. 5. (a) The END model with $0 \leq \theta_l = \theta_r < \pi/2$. (b) The LSS map.

trajectory of the LoG minimums on (s_v, σ_v) . The point (s_v, σ_v) is determined by the equation

$$\begin{cases} \dot{M}_\sigma(s) = 0 \\ \dot{M}_\sigma(s) = 0. \end{cases} \quad (24)$$

Due to the equation's complexity, it is difficult to calculate and find (s_v, σ_v) .

Property 3.3. For the isolated END model with $0 \leq \theta_l + \theta_r < \pi$, $-\pi/2 < \theta_l < \theta_r < \pi/2$, and a corner separation w , two trajectories of the corners are produced by $\sigma^2 = F_1(s)$. They move toward each other as σ increases. The LoG trajectory of the strong corner persists and is asymptotically stationary at s_p . Also, the LoG trajectory of the weak corner terminates at some scale σ_v where it meets the other trajectory consisting of the minimums of $M_\sigma(s)$.

The case $0 \leq \theta_l = \theta_r < \pi/2$ can be regarded as the limit case of the case $0 \leq \theta_l + \theta_r < \pi$ and $-\pi/2 < \theta_l < \theta_r < \pi/2$ when θ_l increases towards θ_r . As θ_l increases, s_p and s_v move towards towards each other. In this process, the LSS map of the case $0 \leq \theta_l + \theta_r < \pi$ and $-\pi/2 < \theta_l < \theta_r < \pi/2$ gradually approaches the case $0 \leq \theta_r = \theta_l < \pi/2$. Eventually, as $0 \leq \theta_r = \theta_l < \pi/2$, $s_v = s_p$ and the trajectories produced by $\sigma^2 = F_1(s)$ merge at $(0.5w, \sigma_m)$ and persist at all scales. The LSS map of the case $0 \leq \theta_r = \theta_l < \pi/2$ is shown in Fig. 5b. The two solid lines are symmetrical with respect to the midpoint $s = 0.5w$ and the dashed line follows the midpoint at all scales. This is consistent with the fact that the corner model in this case is symmetrical as shown in Fig. 5a. Moreover, the location $(0.5w, \sigma_m)$ is solved by calculating the limit of $\sigma^2 = F_1(s)$ at $s = 0.5w$. Apparently, the merging scale $\sigma_m = w/\sqrt{2(1 + \sin\theta)}$ is determined by θ when w is fixed. Here, $\theta = \theta_l = \theta_r$. This indicates that σ_m is a monotonically decreasing function of θ .

Property 3.4. For the isolated END model with $0 \leq \theta_l = \theta_r < \pi/2$ and a corner separation w , the LSS map is produced by $\sigma^2 = F_1(s)$ and symmetrical with respect to $s = 0.5w$. Two LoG trajectories move toward each other as σ increases from 0 to σ_m . For $\sigma \geq \sigma_m$, the two trajectories merge into a single and persistent LoG trajectory.

The case $-\pi < \theta_l + \theta_r < 0$, $-\pi/2 < \theta_l < \theta_r < \pi/2$ is significantly different from the case $0 \leq \theta_l + \theta_r < \pi$, $-\pi/2 < \theta_l < \theta_r < \pi/2$ as shown in Fig. 6b, though their properties are almost the same. The LSS map of the case $-\pi < \theta_l + \theta_r < 0$, $-\pi/2 < \theta_l < \theta_r < \pi/2$ is produced by

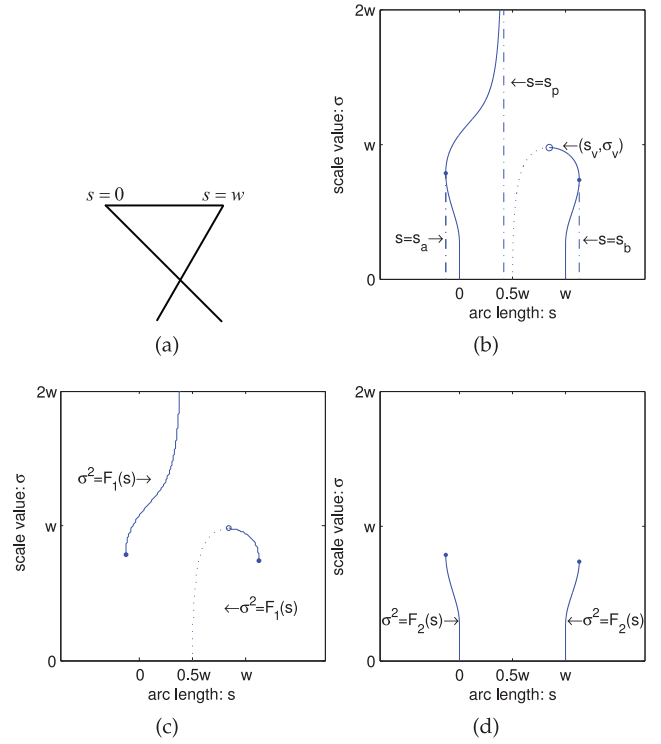


Fig. 6. (a) The END model with $-\pi < \theta_l + \theta_r < 0$ and $-\pi/2 < \theta_l < \theta_r < \pi/2$. (b) The LSS map. (c) The trajectory produced by $\sigma^2 = F_1(s)$. (d) The trajectory produced by $\sigma^2 = F_2(s)$.

$\sigma^2 = F_2(s)$ and $\sigma^2 = F_1(s)$ together instead of only by $\sigma^2 = F_1(s)$. As you can observe, the trajectories produced by $\sigma^2 = F_1(s)$ and $\sigma^2 = F_2(s)$ are drawn in Fig. 6c and Fig. 6d separately. As can be seen in Fig. 6b, $F_2(s)$ is monotonically decreasing on $(s_a, 0)$ and monotonically increasing on (w, s_b) . The consequence is that the trajectories produced by $\sigma^2 = F_2(s)$ move away from the midpoint. Meanwhile, $F_1(s)$ is monotonically increasing on (s_a, s_p) and $(0.5w, s_b)$ and then the trajectory of the weak corner produced by $\sigma^2 = F_1(s)$ moves towards the midpoint as shown in Fig. 6c.

Property 3.5. For the isolated END model with $-\pi < \theta_l + \theta_r < 0$, $-\pi/2 < \theta_l < \theta_r < \pi/2$ and a corner separation w , the LoG trajectories moving away from the corner model midpoint are produced by $\sigma^2 = F_2(s)$; the LoG trajectories moving toward each other are produced by $\sigma^2 = F_1(s)$. The LoG trajectory of the strong corner persists and is asymptotically stationary at s_p whereas the LoG trajectory of the weak corner terminates at scale σ_v and meets the trajectory consisting of the minimums of $M_\sigma(s)$.

The case $-\pi/2 < \theta_l = \theta_r < 0$ can also be viewed as the limit case of the case $-\pi < \theta_l + \theta_r < 0$, $-\pi/2 < \theta_l < \theta_r < \pi/2$. When θ_l increases towards θ_r , there exists a similar process to the one discussed in the case $0 \leq \theta_l = \theta_r < \pi/2$. In this case, $F_1(s)$ and $F_2(s)$ are symmetrical with respect to $s = 0.5w$, which results in the symmetry of the LSS map. As can be seen in Fig. 7d, the trajectories produced by $\sigma^2 = F_2(s)$ repel from each other. Where as in Fig. 7c, the trajectories produced by $\sigma^2 = F_1(s)$ attract each other and merge at $(0.5w, \sigma_m)$. Then in Fig. 7b, the trajectories produced by $\sigma^2 = F_1(s)$ and $\sigma^2 = F_2(s)$ form a mushroom shape. It can be noted that the trajectory of the LoG

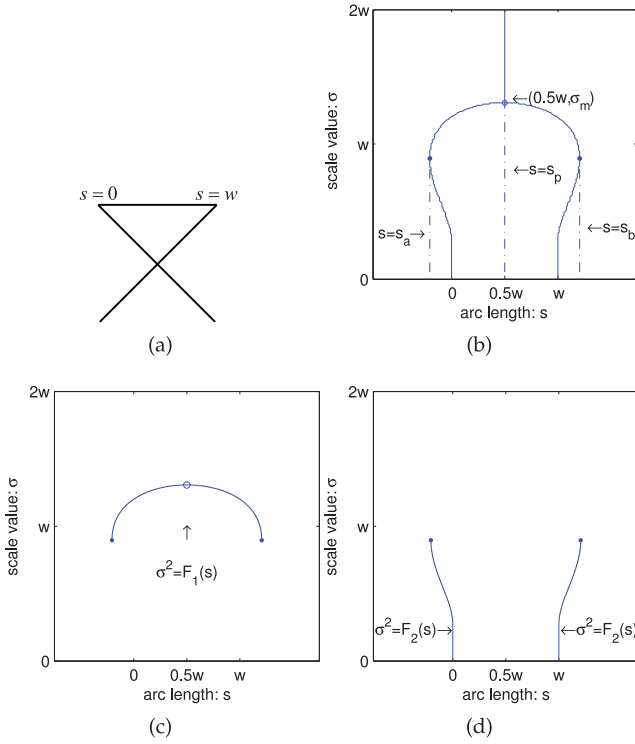


Fig. 7. (a) The END model with $-\pi/2 < \theta_l = \theta_r < 0$. (b) the LSS map. (c) The trajectory produced by $\sigma^2 = F_1(s)$. (d) The trajectory produced by $\sigma^2 = F_2(s)$.

minimums is at $s = 0.5w$ and vanishes where it meets the trajectories of the two corners.

Property 3.6. For the isolated END model with $-\pi/2 < \theta_l = \theta_r < 0$ and a corner separation w , the LSS map is symmetrical with respect to $s = 0.5w$. As σ increases from 0 to σ_m , $\sigma^2 = F_2(s)$ produces two LoG trajectories which move away from the midpoint of the corner model. At the same time, $\sigma^2 = F_1(s)$ produces two trajectories which move toward each other. For $\sigma \geq \sigma_m$, the two trajectories produced by $\sigma^2 = F_1(s)$ merge into a single and persistent LoG trajectory.

3.3 STAIR Model

Similarly to the END model, we obtain the corollary of the STAIR model according to Theorem 2.1 and the domains of $\sigma^2 = F_1(s)$ and $\sigma^2 = F_2(s)$.

Corollary 3.7. For the isolated STAIR model with $-\pi/2 < \theta_l \leq (\pi - \theta_r) < \pi/2$ and a corner separation w , its LSS map is determined by:

$$1) \quad \text{as } 0 \leq \theta_l + (\pi - \theta_r) < \pi, \quad \begin{aligned} \sigma^2 &= F_1(s), & s &\in (0.5w, s_b] \\ \sigma^2 &= F_2(s), & s &\in (s_p, 0) \cup (w, s_b]; \end{aligned} \quad (25)$$

$$2) \quad \text{as } -\pi/2 < \theta_l = (\pi - \theta_r) < \pi/2, \quad \begin{aligned} \sigma^2 &= F_1(s), & s &\in (-\infty, 0) \cup (w, +\infty) \\ \sigma^2 &= (0, +\infty), & s &= 0.5w; \end{aligned} \quad (26)$$

$$3) \quad \text{and as } -\pi < \theta_l + (\pi - \theta_r) < 0, \quad \begin{aligned} \sigma^2 &= F_1(s), & s &\in [s_a, s_p) \cup (0.5w, s_b] \\ \sigma^2 &= F_2(s), & s &\in [s_a, s_p) \cup (s_p, 0) \cup (w, s_b]. \end{aligned} \quad (27)$$

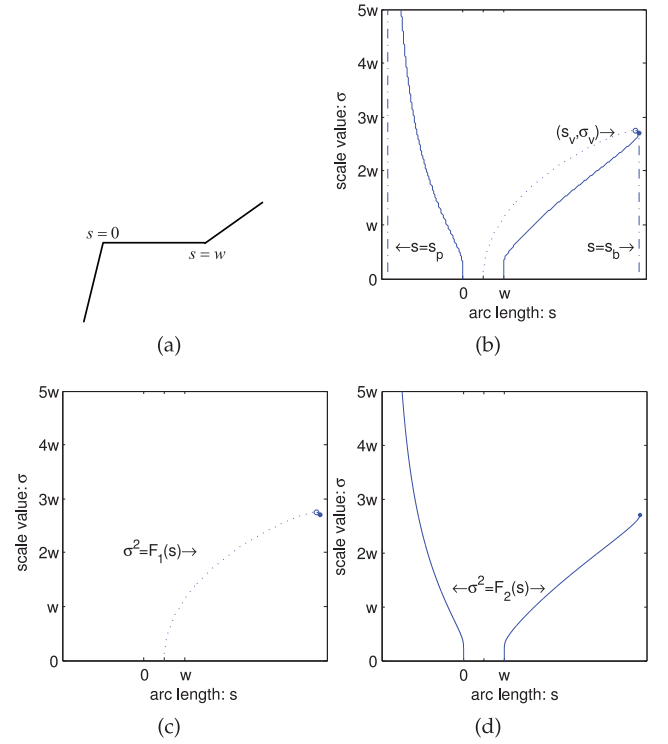


Fig. 8. (a) The STAIR model with $0 \leq \theta_l + (\pi - \theta_r) < \pi$ and $-\pi/2 < \theta_l < (\pi - \theta_r) < \pi/2$. (b) The LSS map. (c) The trajectory produced by $\sigma^2 = F_1(s)$. (d) The trajectory produced by $\sigma^2 = F_2(s)$.

For the case $0 \leq \theta_l + (\pi - \theta_r) < \pi$, $-\pi/2 < \theta_l < (\pi - \theta_r) < \pi/2$ the LSS map exhibits distinctive patterns as shown in Fig. 8. First, as shown in Fig. 8d, the trajectory of the corner $s = 0$ is only produced by $\sigma^2 = F_2(s)$. This trajectory moves away from $s = 0.5w$ and persists at $s = s_p$. Second, as shown in Fig. 8d the trajectory of the corner $s = w$ is mainly produced by $\sigma^2 = F_2(s)$. Meanwhile in Fig. 8c, a very small segment which merges with the LoG minimums at $s = s_v$ is produced by $\sigma^2 = F_1(s)$.

Property 3.8. For the isolated STAIR model with $0 \leq \theta_l + (\pi - \theta_r) < \pi$, $-\pi/2 < \theta_l < (\pi - \theta_r) < \pi/2$, and a corner separation w , the LoG trajectories of the two corners move away from the midpoint of the corner model as σ increases. The LoG trajectory of the strong corner produced by $\sigma^2 = F_2(s)$ persists and is asymptotically stationary at s_p . Meanwhile, the LoG trajectory of the weak corner produced by $\sigma^2 = F_1(s)$ and $\sigma^2 = F_2(s)$ moves toward the midpoint of the corner model again at some scale. Then, it terminates at the scale σ_v and meets the trajectory consisting of the minimums of $M_\sigma(s)$.

Similarly to the cases of the END model, the case $-\pi/2 < \theta_l = (\pi - \theta_r) < \pi/2$ can also be seen as the limit case of the case $0 \leq \theta_l + (\pi - \theta_r) < \pi$, $\pi/2 < \theta_l < (\pi - \theta_r) < \pi/2$. As in the last case, θ_r increases continually, the LSS map will change accordingly. When $-\pi/2 < \theta_l = (\pi - \theta_r) < \pi/2$, the LSS map exhibits a unique pattern as shown in Fig. 9. By Corollary 3.7, the trajectories of the corners $s = w$ and $s = 0$ are only produced by $\sigma^2 = F_1(s)$ and symmetrical with respect to $s = 0.5w$. In other words, the trajectories of the two corners move away from $s = 0.5w$ at the same speed and persist at all scales.

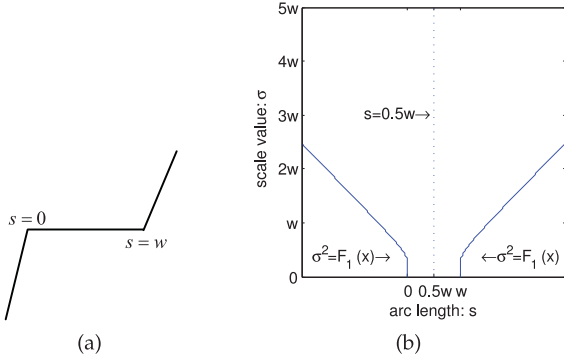


Fig. 9. (a) The STAIR model with $-\pi/2 < \theta_l = (\pi - \theta_r) < \pi/2$. (b) The LSS map.

Property 3.9. For the isolated STAIR model with $-\pi/2 < \theta_l = (\pi - \theta_r) < \pi/2$, and a corner separation w , two trajectories produced by $\sigma^2 = F_1(s)$ are symmetrical with respect to $s = 0.5w$ and repel at the same rate as σ increases.

For $-\pi < \theta_l + (\pi - \theta_r) < 0$, $-\pi/2 < \theta_l < (\pi - \theta_r) < \pi/2$ the LSS map here is slightly different from the case discussed in property 3.5, though they demonstrates the same scale-space behavior as shown in Fig. 10b. Their difference is that the trajectory of the corner on $s = 0$ produced by $\sigma^2 = F_1(s)$ is steeper than the former case. After it reaches $s = s_a$, it will quickly locate at s_p .

Property 3.10. For the isolated STAIR model with $-\pi < \theta_l + (\pi - \theta_r) < 0$, $-\pi/2 < \theta_l < (\pi - \theta_r) < \pi/2$ and a corner separation w , the two LoG trajectories produced by $\sigma^2 = F_2(s)$ move away from the midpoint of the corner model and then the two LoG trajectories produced by $\sigma^2 = F_1(s)$ move toward each other as σ increases. The LoG trajectory of the strong corner persists and is asymptotically stationary at s_p whereas the LoG trajectory of the weak corner terminates at some scale σ_v and meets the trajectory of the LoG minimums.

4 EXPERIMENT AND DISCUSSION

In this section, we will verify the consistence of the Laplacian Scale-Space behavior of corners on a digital curve with its counterpart of a continuous one and then discuss the applications of the derived scale-space properties in this work.

Here, a digital curve will be evolved with the scheme suggested by Zhong [27]. A digital planar curve is obtained by sampling a continuous planar curve $(x(s), y(s))$ onto points $(x_i, y_i), i = 1, 2, \dots$. The digital curve is then evolved by the following iterative process

$$\begin{aligned} x_{i,m+1} &= 0.25x_{i-1,m} + 0.5x_{i,m} + 0.25x_{i+1,m} \\ y_{i,m+1} &= 0.25y_{i-1,m} + 0.5y_{i,m} + 0.25y_{i+1,m}, \end{aligned} \quad (28)$$

where m is the iteration number. When $m = 0$, $(x_{i,0}, y_{i,0})$ is just the original digital curve (x_i, y_i) .

The response of the LoG operator on a digital curve is then computed with

$$\text{LoG}_{i,m} = (\Delta^2 x_{i,m})^2 + (\Delta^2 y_{i,m})^2. \quad (29)$$

Here, Δ is the first-order central difference operator. Fig. 11 demonstrates a set of models and their digital LSS maps

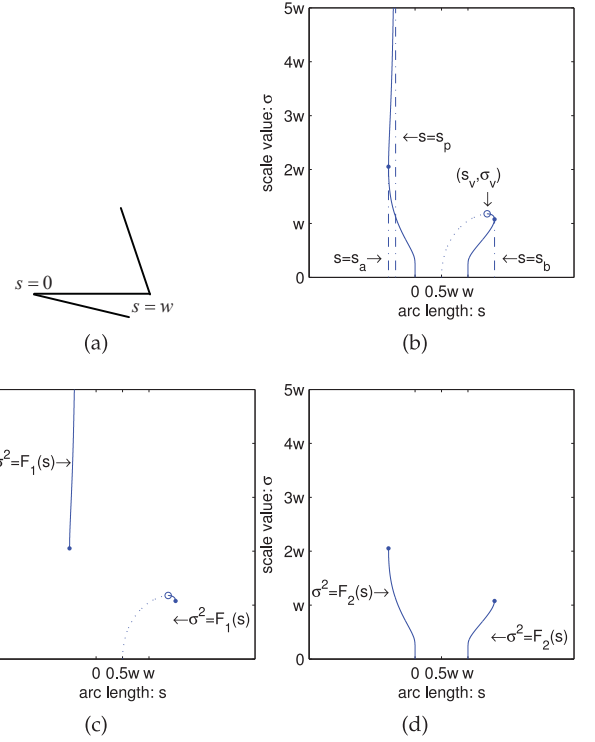


Fig. 10. (a) The STAIR model with $-\pi < \theta_l + (\pi - \theta_r) < 0$ and $-\pi/2 < \theta_l < (\pi - \theta_r) < \pi/2$. (b) The LSS map. (c) The trajectory produced by $\sigma^2 = F_1(s)$. (d) The trajectory produced by $\sigma^2 = F_2(s)$.

computed with Eq. (29). It can be observed that these digital corner models have generally consistent scale-space behavior with their continuous cases.

As stated in the introduction, the LoG operator approximates the DoG operator. Thus, the derived scale-space properties of corners with the LoG operator can be used to investigate the scale-space behavior of corners with the DoG operator. Fig. 12 demonstrates the digital LSS map and the digital DoG map on a closed curve from the Shark image. The digital DoG map is computed by first evolving the digital curve with the above-mentioned iterative process (28) and then gets the evolved curve at each scale by the difference of two successive evolved curves. The number of iterations is set to be half of the number of points on the digital curve to avoid aliasing [19]. It can be easily seen that the digital DoG map is almost the same as the digital LSS map.

Since the scale-space behavior of corners with LoG operator is essentially the same as the one with DoG operator, the LoG operator should have the same corner detection performance as the DoG operator. As an example of the possible application of the derived scale-space properties in this work on corner detection, a novel corner detection algorithm is proposed based on the response function of LoG operator $M_\sigma(s)$. The algorithm is summarized as follows:

- 1) Extract edges $C(s)$ from the original image with an edge detector.
- 2) Calculate the response of the contour $C(s)$ at a given scale σ , according to the definition in formula (4).
- 3) Determine the corners by comparing the local extrema of $M_\sigma(s)$ with a pre-threshold.

As [24] has pointed out that the DoG operator employs both the low scale and the high one for detecting the

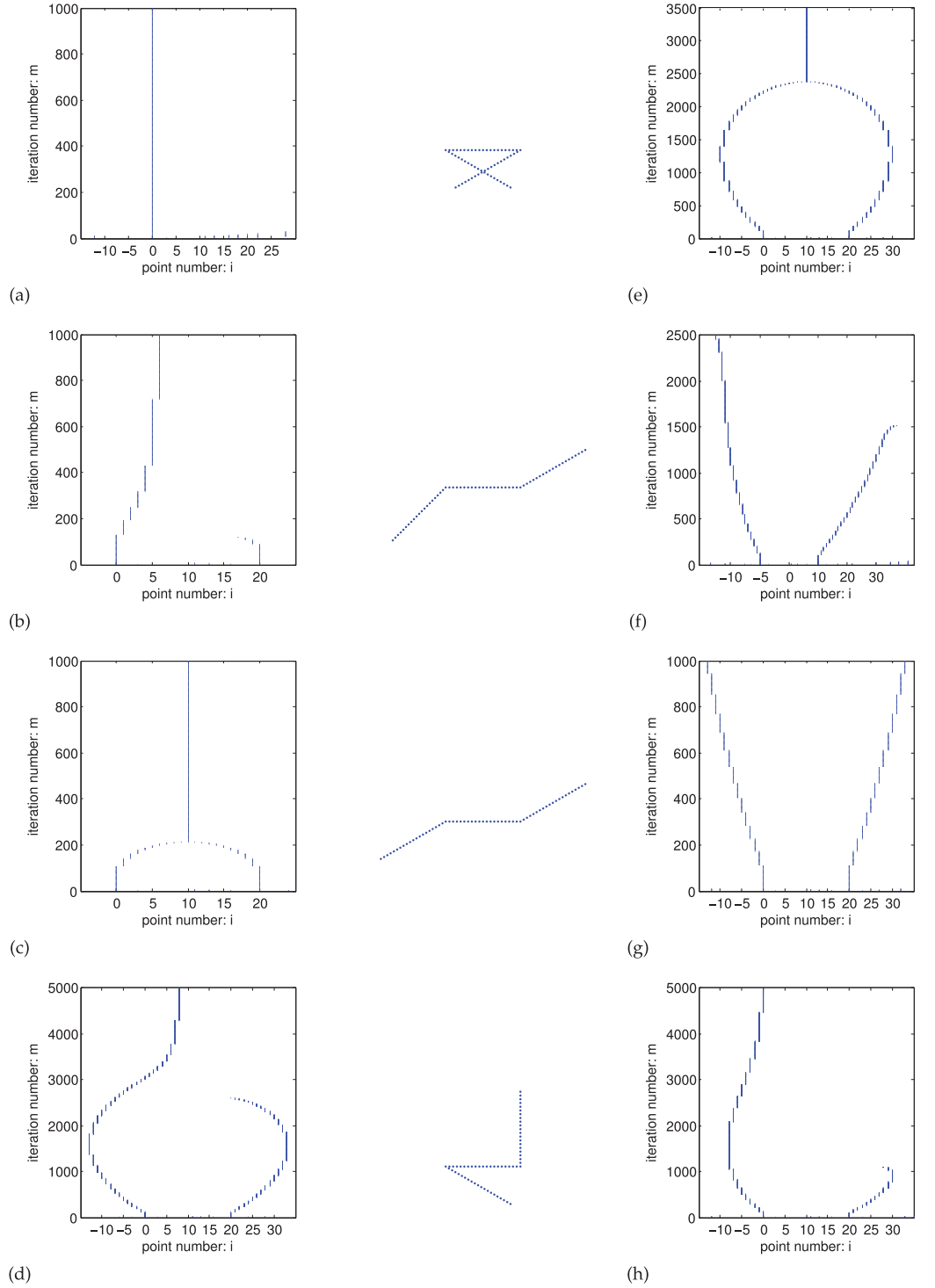


Fig. 11. Various digital corner models and their LSS maps. (a) The Γ model with $\theta_l = \pi/3$. (b) The END model with $\theta_l = \pi/3$ and $\theta_r = 5\pi/12$. (c) The END model with $\theta_l = \pi/3$ and $\theta_r = \pi/3$. (d) The END model with $\theta_l = -5\pi/12$ and $\theta_r = -\pi/3$. (e) The END model with $\theta_l = -\pi/3$ and $\theta_r = -\pi/3$. (f) The STAIR model with $\theta_l = \pi/4$ and $\theta_r = 2\pi/3$. (g) The STAIR model with $\theta_l = \pi/3$ and $\theta_r = 2\pi/3$. (h) The STAIR model with $\theta_l = -\pi/3$ and $\theta_r = \pi$.

candidate corners. Equivalently, the LoG operator intrinsically employs information from multiple scales in the LSS. The advantage is that it is necessary to determine only one scale instead of two as in the DoG operator. In Section 3, we have observed that the strong corner will persist and the weak corner will vanish. Thus, only one proper scale is needed in the proposed algorithm to detect all corners. Moreover, the proposed algorithm has the advantage of low computation complexity. First, according to the definition

of the response, a LoG operator can be pre-computed analytically and applied directly on the boundaries instead of calculating and smoothing the derivative of boundaries. Second, the definition of LoG operator is simple. In fact, except for the convolution of a LoG operator and boundary coordinates, which have the same computational burden as the convolution of Gaussian and boundary coordinates, the response function has only two multiplication operations. In other words, these two attributes lead to the lowest

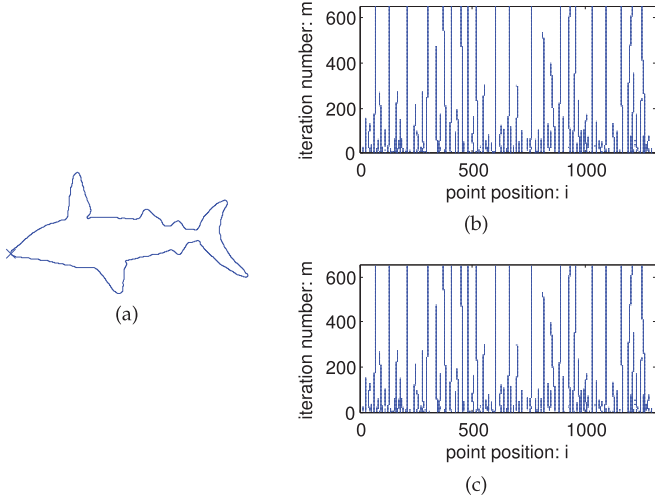


Fig. 12. The digital LSS map and DoG map of key image. (a) The boundary of the Key image. The digitized samples along the curve are taken in a clockwise direction and the start point is indicated by a “x”. (b) LSS map. (c) DoG map.

computational complexity among the existing classical boundary-based corner detection algorithm, such as CSS [20], wavelet [30], covariance matrices [31] and CPDA [23], etc. In Fig. 13, we present some corner detection results of the proposed corner detection algorithm on several images which are usually used for corner detection.

5 CONCLUSION

In this paper, we have presented an analysis of the scale-space behavior of corners with LSS based on a unified corner model. Most of the properties of the LSS are mathematically formulated. Compared with other scale spaces, there are no cusp points [27] in the LSS maps and the properties of different models are expressed consistently. An experiment is conducted to demonstrate the consistence of the continuous case and the digital case.

The proposed Laplacian Scale-Space theory enriches the scale-space theory on the planar curve. It then facilitates the design and improvement of related shape descriptions and corner detection methods. As an example, we have proposed a corner detection algorithm based on the scale-space properties of LSS. It also demonstrates the alternative contour-based scale-space approaches. In fact, due to the relationship between the DoG and the LoG operators, we can easily infer the scale-space behavior of corners with DoG.

APPENDIX

In the following, we will derive the mathematical expressions of LSS map of the corner model by investigating

$$\dot{M}_\sigma(s) = 0. \quad (30)$$

Substitute

$$\begin{aligned} x(s) &= \begin{cases} s \sin \theta_l, & s < 0 \\ s, & 0 \leq s < w \\ (s - w) \sin \theta_r + w, & s \geq w, \end{cases} \\ y(s) &= \begin{cases} s \cos \theta_l, & s < 0 \\ 0, & 0 \leq s < w \\ -(s - w) \cos \theta_r + w, & s \geq w \end{cases} \end{aligned} \quad (31)$$

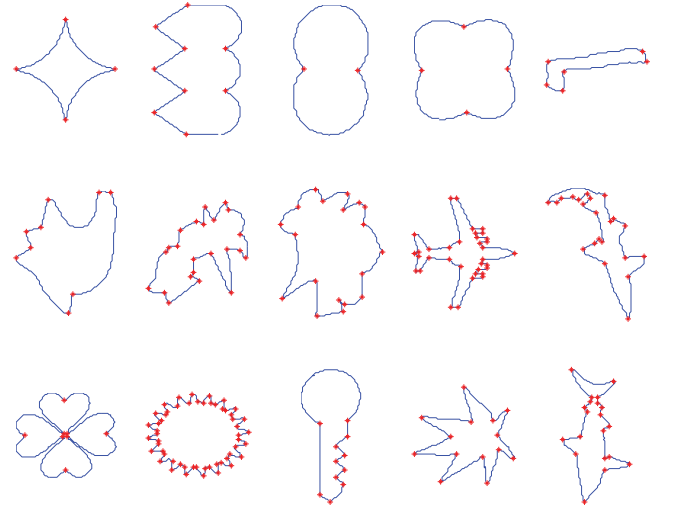


Fig. 13. Some results of the LoG corner detector on several images that are usually used for corner detection.

into $M_\sigma(s)$, then

$$M_\sigma(s) = 2\{\alpha g_\sigma^2(s) + \beta g_\sigma(s)g_\sigma(s - w) + \gamma g_\sigma^2(s - w)\}, \quad (32)$$

where

$$\alpha = 1 - \sin \theta_l, \gamma = 1 - \sin \theta_r, \theta = \frac{\theta_l + \theta_r}{2}, \beta = 2 \sin \theta \sqrt{\alpha \gamma}. \quad (33)$$

Then, (30) becomes

$$2\alpha s g_\sigma^2(s) + \beta(2s - w)g_\sigma(s)g_\sigma(s - w) = 0. \quad (34)$$

Denote

$$\lambda(s, \sigma) = \frac{g_\sigma(s)}{g_\sigma(s - w)} \sqrt{\frac{\alpha}{\gamma}} = \exp\left\{-\frac{(2s - w)\theta}{2\sigma^2}\right\} \sqrt{\frac{1 - \sin \theta_l}{1 - \sin \theta_r}}, \quad (35)$$

and then, (34) is written as

$$s\lambda^2(s, \sigma) + (2s - w) \sin \theta \lambda(s, \sigma) + (s - w) = 0. \quad (36)$$

Solve equation (36) and we get

$$\lambda(s, \sigma) = \frac{(w - 2s) \sin \theta \pm \sqrt{(w - 2s)^2 \sin^2 \theta - 4s(s - w)}}{2s}. \quad (37)$$

Substitute (35) into (37), then we obtain

$$\sigma^2 = \frac{(w - 2s)w}{2 \ln \left[\sqrt{\frac{1 - \sin \theta_r}{1 - \sin \theta_l}} \frac{(w - 2s) \sin \theta \pm \sqrt{(w - 2s)^2 \sin^2 \theta - 4s(s - w)}}{2s} \right]}. \quad (38)$$

Note that in our derivation, two special cases were ignored temporarily. First, when $\theta_l = \theta_r \in (-\pi/2, \pi/2)$ or $\theta_l = (\pi - \theta_r) \in (-\pi/2, \pi/2)$, $s = 0.5w$ is the solution of (30). That is, $\dot{M}_\sigma(0.5w) = 0$ when $\theta_l = \theta_r$ or $\theta_l = (\pi - \theta_r)$. Second, when $\theta_r = \pi/2$ and $\theta_l \in (-\pi/2, \pi/2)$, $s = 0$ is the unique solution of (30).

As previously mentioned, the LSS map consists of s which meets the condition (30). It is easily seen from the formula (38) that these two special cases are equivalent to condition (34). In other words, if we plot them on $s - \sigma$ plane, we get the LSS map.

For $F_1(s)$, solve the inequality

$$\begin{cases} \Delta \geq 0 \\ \varphi > 1 \\ \chi > 0 \end{cases} \quad \text{or} \quad \begin{cases} \Delta \geq 0 \\ 0 < \varphi < 1 \\ \chi < 0, \end{cases} \quad (39)$$

then we get its domain:

$$\text{as } 0 \leq \theta_l + \theta_r < \pi,$$

$$s \in \begin{cases} (0, s_p) \cup (0.5w, w) & \theta_l < \theta_r \\ (0, 0.5w) \cup (0.5w, w) & \theta_l = \theta_r \\ (0, 0.5w) \cup (s_p, w) & \theta_l > \theta_r; \end{cases} \quad (40)$$

$$\text{as } -\pi < \theta_l + \theta_r < 0,$$

$$s \in \begin{cases} [s_a, 0) \cup (0, s_p) \cup (0.5w, w) \cup (w, s_b] & \theta_l < \theta_r \\ [s_a, 0) \cup (0, 0.5w) \cup (0.5w, w) \cup (w, s_b] & \theta_l = \theta_r \\ [s_a, 0) \cup (0, 0.5w) \cup (s_p, w) \cup (w, s_b) & \theta_l > \theta_r; \end{cases} \quad (41)$$

$$\text{as } 0 \leq \theta_l + (\pi - \theta_r) < \pi,$$

$$s \in \begin{cases} (0.5w, s_b] & \theta < \pi - \theta_r \\ (-\infty, 0) \cup (w, +\infty) & \theta_l = \pi - \theta_r \\ [s_b, 0.5w] & \theta_l > \pi - \theta_r; \end{cases} \quad (42)$$

$$\text{and as } -\pi < \theta_l + (\pi - \theta_r) < 0,$$

$$s \in \begin{cases} [s_a, s_p) \cup (0.5w, s_b] & \theta_l < \pi - \theta_r \\ (-\infty, 0) \cup (w, +\infty) & \theta_l = \pi - \theta_r \\ [s_b, 0.5w] \cup (s_p, s_a) & \theta_l > \pi - \theta_r. \end{cases} \quad (43)$$

Note that s_l and s_r are derived from $\Delta = 0$, while s_p is derived from either $\varphi = 1$ or $\psi = 1$.

Similarly to $F_1(s)$, for $F_2(s)$ we solve

$$\begin{cases} \Delta \geq 0 \\ \psi > 1 \\ \chi > 0 \end{cases} \quad \text{or} \quad \begin{cases} \Delta \geq 0 \\ 0 < \psi < 1, \\ \chi < 0 \end{cases} \quad (44)$$

and get the domains of $F_2(s)$:

$$\text{as } 0 \leq \theta_l + \theta_r < \pi,$$

$$s \in \emptyset; \quad (45)$$

$$\text{as } -\pi < \theta_l + \theta_r < 0,$$

$$s \in [s_a, 0) \cup (w, s_b]; \quad (46)$$

$$\text{as } 0 \leq \theta_l + (\pi - \theta_r) < \pi,$$

$$s \in \begin{cases} (s_p, 0) \cup (w, s_b] & \theta_l < \pi - \theta_r \\ \emptyset & \theta_l = \pi - \theta_r \\ [s_b, 0) \cup [w, s_p) & \theta_l > \pi - \theta_r; \end{cases} \quad (47)$$

$$\text{and as } -\pi < \theta_l + (\pi - \theta_r) < 0,$$

$$s \in \begin{cases} [s_a, s_p) \cup (s_p, 0) \cup (w, s_b] & \theta_l < \pi - \theta_r \\ \emptyset & \theta_l = \pi - \theta_r \\ [s_b, 0) \cup [w, s_p) \cup (s_p, s_a) & \theta_l > \pi - \theta_r, \end{cases} \quad (48)$$

where

$$\begin{aligned} s_p &= \frac{w}{2} \left(1 + \frac{\sin \frac{\theta_l + \theta_r}{2}}{\cos \frac{\theta_l + \theta_r}{2}} \right), \\ s_a &= \frac{w}{2} \left(1 - \frac{1}{\cos \theta} \right), \\ s_b &= \frac{w}{2} \left(1 + \frac{1}{\cos \theta} \right), \\ \theta &= \frac{\theta_l + \theta_r}{2}. \end{aligned} \quad (49)$$

ACKNOWLEDGMENTS

This work was partially supported by the National Natural Science Foundation of China (Grant no. 61173131, 91118005, 11202249), Program for Changjiang Scholars and Innovative Research Team in University (Grant No. IRT1196) and the Fundamental Research Funds for the Central Universities (Grant Nos. CDJZR12098801 and CDJZR11095501). Xiaohong Zhang is the corresponding author of the article.

REFERENCES

- [1] A. P. Witkin, "Scale-space filtering," in *Proc. Int. Jt. Conf. Artif. Intell.*, vol. 2, 1983, pp. 1019–1022.
- [2] J. J. Koenderink, "The structure of images," *Biol. Cybern.*, vol. 50, no. 5, pp. 363–370, Aug. 1984.
- [3] A. L. Yuille and T. A. Poggio, "Scaling theorems for zero crossings," *IEEE Trans. Pattern Anal. Mach. Intell.*, vol. PAMI-8, no. 1, pp. 15–25, Jan. 1986.
- [4] T. Lindeberg, "Edge detection and ridge detection with automatic scale selection," in *Proc. CVPR IEEE Comput. Soc. Conf. Comput. Vis. Pattern Recognit.*, 1996, pp. 465–470.
- [5] L. Florack and A. Kuijper, "The topological structure of scale-space images," *J. Math. Imaging Vis.*, vol. 12, no. 1, pp. 65–79, Feb. 2000.
- [6] E. Balmashnova, B. Platel, L. Florack, and B. t. H. Romeny, "Object matching in the presence of non-rigid deformations close to similarities," in *Proc. IEEE 11th Int. Conf. Comput. Vis.*, 2007, pp. 1–8.
- [7] G. Bebis, G. Papadourakis, and S. Orphanoudakis, "Curvature scale-space-driven object recognition with an indexing scheme based on artificial neural networks," *Pattern Recognit.*, vol. 32, no. 7, pp. 1175–1201, Jul. 1999.
- [8] C.-C. Chang, "Adaptive multiple sets of CSS features for hand posture recognition," *Neurocomputing*, vol. 69, no. 16–18, pp. 2017–2025, Oct. 2006.
- [9] F. Mokhtarian and S. Abbasi, "Robust automatic selection of optimal views in multi-view free-form object recognition," *Pattern Recognit.*, vol. 38, no. 7, pp. 1021–1031, Jul. 2005.
- [10] M. Cui, P. Wonka, A. Razdan, and J. Hu, "A new image registration scheme based on curvature scale space curve matching," *Vis. Comput.*, vol. 23, no. 8, pp. 607–618, Jun. 2007.
- [11] A. Garrido, N. Pérez de la blanca, and M. Garcia-Silvente, "Boundary simplification using a multiscale dominant-point detection algorithm," *Pattern Recognit.*, vol. 31, no. 6, pp. 791–804, Jun. 1998.
- [12] X. Zabulis, J. Sporring, and S. C. Orphanoudakis, "Perceptually relevant and piecewise linear matching of silhouettes," *Pattern Recognit.*, vol. 38, no. 1, pp. 75–93, Jan. 2005.
- [13] S. Mahmoudi and M. Daoudi, "A probabilistic approach for 3D shape retrieval by characteristic views," *Pattern Recognit. Lett.*, vol. 28, no. 13, pp. 1705–1718, 2007.

- [14] H. Asada and M. Brady, "The curvature primal sketch," *IEEE Trans. Pattern Anal. Mach. Intell.*, vol. PAMI-8, no. 1, pp. 2–14, Jan. 1986.
- [15] F. Mokhtarian and A. Mackworth, "Scale-based description and recognition of planar curves and two-dimensional shapes," *IEEE Trans. Pattern Anal. Mach. Intell.*, vol. PAMI-8, no. 1, pp. 34–43, Jan. 1986.
- [16] F. Mokhtarian and A. Mackworth, "A theory of multiscale, curvature-based shape representation for planar curves," *IEEE Trans. Pattern Anal. Mach. Intell.*, vol. 14, no. 8, pp. 789–805, 1992.
- [17] B. K. Ray and K. S. Ray, "Corner detection using iterative Gaussian smoothing with constant window size," *Pattern Recognit.*, vol. 28, no. 11, pp. 1765–1781, Nov. 1995.
- [18] K. Xin, K. B. Lim, and G. S. Hong, "A scale-space filtering approach for visual feature extraction," *Pattern Recognit.*, vol. 28, no. 8, pp. 1145–1158, Aug. 1995.
- [19] A. Rattarangsi and R. Chin, "Scale-based detection of corners of planar curves," *IEEE Trans. Pattern Anal. Mach. Intell.*, vol. 14, no. 4, pp. 430–449, Apr. 1992.
- [20] F. Mokhtarian and R. Suomela, "Robust image corner detection through curvature scale space," *IEEE Trans. Pattern Anal. Mach. Intell.*, vol. 20, no. 12, pp. 1376–1381, Dec. 1998.
- [21] X. He and N. Yung, "Curvature scale space corner detector with adaptive threshold and dynamic region of support," in *Proc. IEEE 17th Int. Conf. Pattern Recognit.*, vol. 2, 2004, pp. 791–794.
- [22] X. Zhang, M. Lei, D. Yang, Y. Wang, and L. Ma, "Multi-scale curvature product for robust image corner detection in curvature scale space," *Pattern Recognit. Lett.*, vol. 28, no. 5, pp. 545–554, Apr. 2007.
- [23] M. Awrangjeb and G. Lu, "An improved curvature scale-space corner detector and a robust corner matching approach for transformed image identification," *IEEE Trans. Image Process.*, vol. 17, no. 12, pp. 2425–2441, Dec. 2008.
- [24] X. Zhang, H. Wang, M. Hong, L. Xu, D. Yang, and B. C. Lovell, "Robust image corner detection based on scale evolution difference of planar curves," *Pattern Recognit. Lett.*, vol. 30, no. 4, pp. 449–455, Mar. 2009.
- [25] M. Awrangjeb, G. Lu, and C. S. Fraser, "Performance comparisons of contour-based corner detectors," *IEEE Trans. Image Process.*, vol. 21, no. 9, pp. 4167–4179, 2012.
- [26] T. Lindeberg, "Scale selection properties of generalized scale-space interest point detectors," *J. Math. Imaging Vis.*, vol. 46, no. 2, pp. 177–210, Sep. 2012.
- [27] B. Zhong, K.-K. Ma, and W. Liao, "Scale-space behavior of planar-curve corners," *IEEE Trans. Pattern Anal. Mach. Intell.*, vol. 31, no. 8, pp. 1517–1524, Aug. 2009.
- [28] B. Zhong and W. Liao, "Direct curvature scale space: Theory and corner detection," *IEEE Trans. Pattern Anal. Mach. Intell.*, vol. 29, no. 3, pp. 508–512, Mar. 2007.
- [29] B. J. Zhong and C. Li, "Robust image corner detection using curvature product in direct curvature scale space," *Appl. Mech. Mater.*, vol. 20–23, pp. 725–730, Jan. 2010.
- [30] A. Qudus and M. Gabbouj, "Wavelet-based corner detection technique using optimal scale," *Pattern Recognit. Lett.*, vol. 23, no. 1–3, pp. 215–220, Jan. 2002.
- [31] C.-h. Yeh, "Wavelet-based corner detection using eigenvectors of covariance matrices," *Pattern Recognit. Lett.*, vol. 24, no. 15, pp. 2797–2806, Nov. 2003.
- [32] I. C. Paula Jr., F. N. S. Medeiros, F. N. Bezerra, D. M. Ushizima, and I. C. Paula, "Multiscale corner detection in planar shapes," *J. Math. Imaging Vis.*, vol. 45, no. 3, pp. 251–263, Jul. 2012.
- [33] S. Tabbone, "Corner detection using Laplacian of Gaussian operator," in *Proc. Scand. Conf. Image Anal.*, 1993, pp. 1055–1059.
- [34] S. Tabbone, "Detecting junctions using properties of the Laplacian of Gaussian detector," in *Proc. 12th Int. Conf. Pattern Recognit.*, vol. 1, 1994, pp. 52–56.
- [35] T. Lindeberg, "Feature detection with automatic scale selection," *Int. J. Comput. Vis.*, vol. 30, no. 0920–5691, pp. 79–116, 1998.
- [36] D. Lowe, "Object recognition from local scale-invariant features," in *Proc. Seventh IEEE Int. Conf. Comput. Vis.*, 1999, pp. 1150–1157.
- [37] D. G. Lowe, "Distinctive image features from scale-invariant keypoints," *Int. J. Comput. Vis.*, vol. 60, no. 2, pp. 91–110, Nov. 2004.
- [38] K. Mikolajczyk, T. Tuytelaars, C. Schmid, A. Zisserman, J. Matas, F. Schaffalitzky, T. Kadir, and L. V. Gool, "A comparison of affine region detectors," *Int. J. Comput. Vis.*, vol. 65, no. 1–2, pp. 43–72, Oct. 2005.
- [39] S. A. Tabbone, L. Alonso, and D. Ziou, "Behavior of the Laplacian of Gaussian extrema," *J. Math. Imaging Vis.*, vol. 23, no. 1, pp. 107–128, Jul. 2005.



Xiaohong Zhang received the MS degree in applied mathematics from Chongqing University, Chongqing, PR China, where he also received the PhD degree in computer software and theory, in 2006. He is currently a professor in School of Software Engineering at Chongqing University. His current research interests include data mining of software engineering, topic modeling, image semantic analysis and video analysis.



Ying Qu received the BS and MS degrees in applied mathematics from Chongqing Normal University and Chongqing University, Chongqing, PR China, in 2008 and 2012, respectively. He is currently working toward the PhD degree in computer science at the College of Computer Science in Chongqing University. His current research interests include computer vision, pattern recognition, and machine learning.



Dan Yang received the BS, MS, and the PhD degrees from Chongqing University, Chongqing, PR China, in 1982, 1985, and 1997, respectively. He is currently a professor in School of Software Engineering at Chongqing University. His current research interests include data mining of software engineering, topic modeling, image semantic analysis and video analysis.



Hongxing Wang received the BS degree in information and computing science and the MS degree in operational research and cybernetics from Chongqing University, Chongqing, PR China, in 2007 and 2010, respectively. He is currently working toward the PhD degree from Nanyang Technological University, Singapore. His current research interests include computer vision, image and video analysis, and pattern recognition.



computer interfaces.

Jeff Kymer received the BS degree in computer science and the BS degree in mathematics from Westfield State College in Westfield, MA, in 1986. He is currently a senior lecturer in School of Software Engineering at Chongqing University, Chongqing, PR China. He has worked on a range of software products from a top selling CD-Rom (the MPC Wizard) to one of the first multi-track audio boards. His current research interests include software engineering, computational linguistics, teaching, data mining, and alternate

► For more information on this or any other computing topic, please visit our Digital Library at www.computer.org/publications/dlib.